



# Simultaneous dynamic glucose-enhanced (DGE) MRI and fiber photometry measurements of glucose in the healthy mouse brain

Afroditi Eleftheriou<sup>a,b</sup>, Luca Ravotto<sup>a</sup>, Matthias T. Wyss<sup>a,b</sup>, Geoffrey Warnock<sup>a</sup>, Anita Siebert<sup>a</sup>, Moritz Zaiss<sup>c,d</sup>, Bruno Weber<sup>a,b,\*</sup>

<sup>a</sup> University of Zurich, Institute of Pharmacology and Toxicology, Zurich, Switzerland

<sup>b</sup> Neuroscience Center Zurich, University and ETH Zurich, Zurich, Switzerland

<sup>c</sup> Institute of Neuroradiology, University Hospital Erlangen, Friedrich-Alexander University Erlangen Nürnberg, Erlangen, Germany

<sup>d</sup> High-field Magnetic Resonance Center, Max Planck Institute for Biological Cybernetics, Tübingen, Germany

## ARTICLE INFO

### Keywords:

Glucose  
Fiber photometry  
Genetically encoded sensors  
Two-photon microscopy  
Kinetic modeling

## ABSTRACT

Glucose is the main energy source in the brain and its regulated uptake and utilization are important biomarkers of pathological brain function. Glucose Chemical Exchange Saturation Transfer (GlucoseCEST) and its time-resolved version Dynamic Glucose-Enhanced MRI (DGE) are promising approaches to monitor glucose and detect tumors, since they are radioactivity-free, do not require <sup>13</sup>C labeling and are easily translatable to the clinics. The main principle of DGE is clear. However, what remains to be established is to which extent the signal reflects vascular, extracellular or intracellular glucose. To elucidate the compartmental contributions to the DGE signal, we coupled it with FRET-based fiber photometry of genetically encoded sensors, a technique that combines quantitative glucose readout with cellular specificity. The glucose sensor FLIP was used with fiber photometry to measure astrocytic and neuronal glucose changes upon injection of D-glucose, 3OMG and L-glucose, in the anaesthetized murine brain. By correlating the kinetic profiles of the techniques, we demonstrate the presence of a vascular contribution to the signal, especially at early time points after injection. Furthermore, we show that, in the case of the commonly used contrast agent 3OMG, the DGE signal actually anticorrelates with the glucose concentration in neurons and astrocytes.

## 1. Introduction

Tomographic techniques such as Magnetic Resonance Imaging (MRI), Positron Emission Tomography (PET) and Computed Tomography (CT) are widely used in clinical settings to probe brain physiology and pathology. Their strength resides in the possibility to rapidly investigate large volumes at substantial depths in a non-invasive way, allowing for the diagnosis of pathological tissue alterations or the identification of brain areas responsible for specific functions (Herholz et al., 2007; Langen et al., 2017). However, the spatial resolution is limited to the sub-millimeter range even with state-of-the-art technologies (Weiskopf et al., 2021), preventing cell identification and assessment of cell specific contributions to signals. Thus, combining tomographic methods with cell-type specific techniques can produce invaluable complementary information.

A potential candidate for this multimodal approach is fiber photometry, a preclinical method which uses an optic fiber to deliver the exci-

tation light and collect fluorescence from a genetically encoded biosensor (Gunaydin et al., 2014). The surgical implantation of the fiber allows to monitor neuronal activity (Liang et al., 2017), neurotransmitter release (Jones-Tabah et al., 2020; Wang et al., 2021) or metabolic activity (Natsubori et al., 2020) in specific brain areas, including deep subcortical regions, which are not accessible by *in vivo* microscopy techniques, such as two-photon laser scanning microscopy (2PLSM). Fiber photometry does not share the subcellular resolution of 2PLSM but reports the bulk signal from a tissue volume surrounding the fiber tip (Pisanello et al., 2019). However, it maintains the cellular specificity since the genetically encoded biosensor of interest can be expressed in a cell-specific manner.

Concurrent tomographic and photometric measurements have been realized before (Patel et al., 2020; Pradier et al., 2021; Schulz et al., 2012; Yu et al., 2020). For example, Blood Oxygen Level Dependent functional MRI (BOLD fMRI) has been coupled with fiber photometry of fluorescent calcium indicators to study the neuronal contribution to

\* Corresponding author at: University of Zurich, Institute of Pharmacology and Toxicology, Zurich, Switzerland.

E-mail address: [bweber@pharma.uzh.ch](mailto:bweber@pharma.uzh.ch) (B. Weber).

<https://doi.org/10.1016/j.neuroimage.2022.119762>.

Received 14 July 2022; Received in revised form 27 October 2022; Accepted 21 November 2022

Available online 24 November 2022.

1053-8119/© 2022 Published by Elsevier Inc. This is an open access article under the CC BY-NC-ND license (<http://creativecommons.org/licenses/by-nc-nd/4.0/>)

neurovascular coupling by correlation of the intracellular calcium activity to the BOLD response (Schulz et al., 2012). However, so far there are no reports on coupling tomographic techniques with fiber photometry of metabolites, such as glucose, lactate or pyruvate, which are key players in most processes observed with molecular imaging tools. The main difference between the measurement of metabolite levels and calcium or neurotransmitters activity is that the former requires a quantitative fluorescence readout (e.g., ratiometric or lifetime-based), which presents additional challenges as compared to simply monitoring the frequency of transients due to neuronal spiking activity (Yellen and Monjeon, 2015). We coupled fiber photometry of metabolites with Dynamic Glucose-Enhanced (DGE) MRI (Kim et al., 2022; Xu et al., 2015), a time resolved version of Chemical Exchange Saturation Transfer (glucoCEST) MRI, to elucidate the compartmental (vascular, extracellular, intracellular) origin of its signal.

In glucoCEST, the initial saturation of the glucose proton pool is followed by the chemical exchange between glucose and water protons, resulting in a decrease in the water MRI signal proportional to glucose concentration (van Zijl and Yadav, 2011). GlucoCEST has been proposed as a potential alternative to other tomographic techniques for tumor imaging (Chan et al., 2012; Walker-Samuel et al., 2013), since it does not require radioactive tracers, ionizing radiation or  $^{13}\text{C}$ -labelled compounds. In animal research, it has been used to study pathological conditions such as tumours (Rivlin and Navon, 2018; Walker-Samuel et al., 2013; Xu et al., 2020), traumatic brain injury (Tu et al., 2018), Alzheimer's disease (Huang et al., 2020; Tolomeo et al., 2018), hypoxia (Jin et al., 2018), or glucose consumption during neuronal activation (Roussel et al., 2019). For dynamic studies, a time-resolved version has been developed, called Dynamic Glucose-Enhanced (DGE) MRI, that allows for higher temporal resolution by omitting the time-consuming acquisition of full spectra and the signal normalization to an off-resonance chemical shift. DGE MRI has been used to study tumours (Xu et al., 2020), disruption of blood-brain barrier (BBB) (Xu et al., 2015) or Alzheimer's disease (Huang et al., 2020).

To monitor glucose by fiber photometry, we cell-specifically expressed the genetically encoded biosensor FLIIP (Takanaga et al., 2008) (based on Förster Resonance Energy Transfer, or FRET) in the mouse cortex and assessed how astrocytic and neuronal glucose concentration correlates with the DGE signal upon intravenous (IV) administration of D-glucose, 3-O-methyl-D-glucose (3OMG) and L-glucose. 3OMG is a known glucoCEST contrast agent (Rivlin and Navon, 2018) that is transported through the BBB and cellular membranes by the same GLUT transporters as D-glucose. In the cells, 3OMG does not get metabolized, since it is not a substrate for hexokinase. On the other hand, L-glucose does not get transported by the GLUTs through the BBB (Sasaki et al., 2016; Zhao and Keating, 2007) and remains in the vasculature until cleared by the kidneys. Both 3OMG and L-glucose are not detected by the glucose sensor FLIIP. First, we demonstrate the strengths and limitations of fiber photometry of FRET sensors, previously reported only in a very limited number of studies (Jones-Tabah et al., 2021, 2020; Natsubori et al., 2020), by comparison with 2PLSM. After having assessed the reliability of fiber photometry for monitoring glucose changes, we show that the DGE signal does not generally correlate with the intracellular glucose concentration either in neurons or astrocytes. This observation suggests that the DGE signal contains extracellular and vascular contributions in addition to intracellular ones, with a relative importance that depends on the time after glucose injection. In the case of 3OMG, we observe signal dynamics that correspond to trans-acceleration, a phenomenon in which the influx of 3OMG in the cell causes a concomitant efflux of glucose to the extracellular space (Carruthers, 1990; Deng et al., 2014; Widdas, 1952). These transients cannot be resolved by glucoCEST or DGE and are of primary importance for clinical applications. Our approach paves the way for future studies of cell-specific metabolite dynamics in combination with tomographic techniques, which could lead to a better interpretation of tomographic images in clinical contexts.

## 2. Methods

### 2.1. Genetically encoded sensor for glucose

Relative glucose concentration level measurements were performed using the genetically encoded FRET sensor FLIIP<sup>12</sup>Pglu700 $\mu\delta$ 6 (FLIIP) (Takanaga et al., 2008), which contains ECFP as a FRET donor and Citrine as acceptor. The sensor was codon-diversified, to overcome homologous recombination problems (Komatsubara et al., 2015), and expressed in the somatosensory cortex of mice using Adeno-Associated-Viral (AAV) vectors. The cell-specific promoters human Synapsin (hSyn) and the short Glial Fibrillary Acidic Protein (GFAP) were used for expression in neurons and astrocytes, respectively. Viral constructs for expression in neurons and astrocytes were prepared by the UZH Viral Vector Facility using previously published procedures (Paterna et al., 2004). The following physical titers were used for *in vivo* expression: hSyn1/FLIIP,  $9 \times 10^{11}$  vg/ml; GFAP/FLIIP,  $5.7 \times 10^{11}$  vg/ml. The injected volume was 230  $\mu\text{l}$  per injection site.

### 2.2. Animals

All experimental procedures were approved by the Veterinary Office of the Canton of Zurich and done in accordance with its guidelines. Twenty female wild-type mice (C57BL/6 J; Charles Rivers) of age 3–8 months were used for simultaneous DGE and fiber photometry measurements of glucose and six were used for two-photon laser scanning microscopy (2PLSM) imaging. Female mice were chosen due to reduced conflictuality during housing, as sex is not a relevant variable for MRI signal interpretation. Animals were housed in groups of five at an inverted 12 h–12 h light-dark cycle with food and water ad libitum and were given at least 1 week to acclimatize to their housing before experimentation. In all protocols, we indicate with *n* the number of experiments and with *N* the number of mice.

### 2.3. Anaesthesia

For induction of anesthesia, 4% isoflurane was used in a mixture of oxygen and medical air. During surgery, mice were kept anesthetized with 2% isoflurane and the analgesic Buprenorphine (2 mg/kg) was delivered subcutaneously half an hour before stopping the isoflurane supply. During imaging, mice were kept under anesthesia with 1.5% isoflurane and the breathing rate was monitored and kept at around 55–65 breaths per minute. The core temperature was monitored and modulated at  $37 \pm 0.5$  °C. During 2PLSM imaging, the temperature modulation was done with a rectal probe and a heating blanket (Harvard Apparatus), while during MRI and fiber photometry measurements a bed-integrated tubing with circulating water was used.

### 2.4. Surgical procedures for fiber photometry and 2PLSM

Mice were anaesthetized and placed in a stereotactic frame. An incision was made at the top of the head. A bonding agent (ONE COAT 7 UNIVERSAL; Coltene) was applied to the cleaned skull and polymerized using a blue light source (Dental WOODPECKER® curing light LED-F). A custom-made aluminum or PEEK head post was connected with MR-compatible blue-light curable dental cement (IPS Empress Direct Effect; Ivoclar vivadent AG) to the skull, creating a “cap”, for later reproducible fixation under the two-photon microscope or in the MRI animal bed, respectively. The open skin was glued on the dental cement cap and antibiotic cream (Fucidin® 20 mg/1 g; LEO) was applied on the edges to prevent infection. Two days after the head-post surgery, a  $2 \times 2$  mm<sup>2</sup> or a  $3.5 \times 3.5$  mm<sup>2</sup> craniotomy was performed, for optic fiber implantation or glass plate placement, respectively, above the somatosensory neocortex, using a dental drill (Bien-Air) and solution containing viral vector was injected into the primary somatosensory cortex at 300  $\mu\text{m}$

to 350  $\mu\text{m}$  under the surface of the brain using a custom-made microinjection pump. An optic fiber implant (see below) or a  $3 \times 3 \text{ mm}^2$  square sapphire glass plate (POWATEC GmbH) was placed over the brain and glued to the skull using dental cement, according to published protocols (Holtmaat et al., 2009). Mice were allowed to recover for three weeks before imaging.

## 2.5. Fiber photometry

Fluorescence recordings reflecting intracellular glucose changes were performed using a custom-built fiber photometry setup optimized for Förster Resonance Energy Transfer (FRET) biosensors.

The setup consists of a 430 nm LED source (THORLABS, M430L4), driven by an LED driver that allows for external modulation (THORLABS, LEDD1B). The LED light is collimated using a lens with focal length 20 mm (THORLABS, ACL2520U-A). A band pass filter,  $430 \pm 2 \text{ nm}$  with FWHM  $10 \pm 2 \text{ nm}$  (THORLABS, FB430-10), is used to narrow the excitation bandwidth and a long pass dichroic mirror, 455 nm (AHF, F48-455), is used to guide the excitation light into a fiber coupled collimator (THORLABS, F950FC-A). A 5 m long optic fiber with diameter 400  $\mu\text{m}$  (Doric, MFP\_400/440/1100-0.37\_5m\_FC-ZF1.25\_LAF) is connected to the fiber coupled collimator. The other end of the optic fiber is connected using a “mating sleeve” (THORLABS, ADAL1) to a ceramic ferrule (THORLABS CFLC440-10) that is permanently attached to the mouse skull. The optic fiber implant was polished using a commercial fiber polishing kit (THORLABS, FN96A).

The excitation light was modulated to achieve an average power at the brain surface of about 150  $\mu\text{W}$  for astrocytic and 75  $\mu\text{W}$  for neuronal measurements. The emitted light is transmitted through the same optic fiber as the excitation light, passes through the 455 nm dichroic mirror and is further filtered with a long pass 460 nm filter (AHF, F47-461) to remove residual excitation light. The remaining light is split by a long pass 515 nm dichroic mirror (AHF, F33-515A) and focused into two detectors (HAMAMATSU, H9305-03) using 30 mm focal length lenses (THORLABS, LA1805-A - N-BK7). Additional bandpass filters were positioned in front of the detectors: 475/42 nm for the CFP channel (AHF, F39-476) and 530/43 nm for the YFP channel (AHF, F37-535). See Supplementary Fig. 1 for a detailed scheme of the setup.

To minimize the optic fiber autofluorescence signal contribution, a low autofluorescence optic fiber was used and was photobleached overnight before each measurement. The photobleaching protocol used was the same as the acquisition protocol and adequate photobleaching time assured that the data acquisition was taking place in the plateau phase of the photobleaching temporal profile.

The fiber photometry setup was operated using a custom-written C++ software (courtesy of Prof. Sergei Vinogradov). The excitation light was modulated using a square pulse ON-OFF function with 100 ms step. The OFF signal of the pulses was subtracted from the ON signal to remove electronic noise and stray light contributions.

The dynamic curves of the fiber photometry measurements were calculated as the ratio of the YFP signal divided by the CFP signal. Both channels were previously corrected by removing fiber autofluorescence (Supplementary Fig. 2), measured immediately before the experiment. The ratio values were normalized to the mean of the first 10 min of measurements.

## 2.6. Two-photon laser scanning microscopy

The 2PLSM images were acquired with a custom-made two-photon microscope (Mayrhofer et al., 2015) coupled to a fs pulsed laser with pulse width  $< 120 \text{ fs}$  (InSight DeepSee Dual; Spectra-Physics) and a 16x water immersion objective (Nikon N16XLWD-PF, 0.8 NA, 3 mm WD). The sensor was excited at 870 nm and the emitted light collected using a set of 3 dichroics (F73-825, F38-560, F38-506; AHF Analysentechnik) and focused (LA1050-A1 and AL5040-A2; Thorlabs) on two PMTs (H9305-03, Hamamatsu), equipped with bandpass filters for CFP

(475/50, AHF Analysentechnik) and YFP (542/50, AHF Analysentechnik) detection. The microscope was operated using a custom-written software based on ScanImage (Version 3.8) (Pologruto et al., 2003) and LabView (National Instruments).

The 2PLSM dynamic curves were acquired with a time resolution of 10 s and their ratio calculated as the mean value of the YFP image divided by the mean value of the CFP one, and later normalized to the mean of the 10 min baseline. This procedure is justified by the uniformity of the ratio values all over the imaged planes and minimizes errors due to noise in single pixels (Wang, 2007).

## 2.7. MRI acquisition

*In vivo* DGE measurements were performed on a 7T Bruker BioSpec 70/30 animal MRI scanner. A birdcage coil (RF RES 300 1H 112/086 QSN TO AD, Bruker Biosystems) was used for RF transmission and a custom-made surface coil was used for receiving the RF.

Alterations were done on the standard Bruker MRI mouse bed to allow for reproducible fixation of the mouse, using a PEEK “bridge” with a grooved hole for headpost attachment. A 3D printed holder was used to hold the surface coil in place (Fig. 1).

A stack of nine T2 RARE anatomical images of the brain (slice thickness 1 mm, acquisition matrix  $196 \times 128$  pixels, resolution  $0.06 \times 0.06 \text{ mm/pixel}$ , RARE factor 8, TR 2.5 s, TE 43.01 ms) were acquired to identify the slice with the optic fiber implant (Fig. 1).

The DGE images were acquired on the brain slice with the fiber implant with a T2 single-shot RARE sequence (slice thickness 1 mm, acquisition matrix  $98 \times 64$  pixels, resolution  $0.12 \times 0.12 \text{ mm/pixel}$ , RARE factor 64, TR 4 s, TE 5.16 ms). For each time point 9 images were acquired, each after a 1-s pre-saturation block pulse of  $B_1 = 3 \mu\text{T}$  at the hydroxyl proton frequency offsets:  $\pm 2 \text{ ppm}$ ,  $\pm 1.5 \text{ ppm}$ ,  $\pm 1.2 \text{ ppm}$ ,  $\pm 0.9 \text{ ppm}$  and 0 ppm from the water peak. A total of 150 time points were acquired, with a temporal resolution of 36 s.

The DGE images were calculated as the negative of the intensity at 1.2 ppm, normalized to the mean of the 10 min baseline. The negative values were chosen for clarity, so that an increase in signal would correspond to an increase in glucose concentration. The data are corrected for motion and for B0 inhomogeneities. To achieve high temporal resolution, we did not use the commonly used Water Saturation Shift Referencing (WASSR) method for B0 correction. The B0 map used for the B0 correction is calculated by finding the minimum of the interpolated z-spectrum of each pixel of each time point and calculating the difference from the water peak at zero (Anemone et al., 2021). Time smoothing (boxcar averaging kernel) based on a window of 5 time points was applied to reduce noise. For visualization purposes only, a window of 41 time points was used for images.

For the analysis of ROI data, we compared three commonly adopted ways of analysis. The difference  $I(-1.2 \text{ ppm}) - I(1.2 \text{ ppm})$  and the ratio  $I(-1.2 \text{ ppm})/I(1.2 \text{ ppm})$  have both higher noise than the single intensity value  $-I(1.2 \text{ ppm})$ , but are less prone to systematic errors. Our conclusions do not depend on the chosen analysis method. In the main text, we chose to use the negative intensity at 1.2 ppm since it shows the highest variation and lowest noise (Zaiss et al., 2019a), but the results for all methods are shown in the supplementary figures. To further exclude potential systematic errors due to frequency drift caused by gradient coil heating or mechanical vibration (Foerster et al., 2005; Lange et al., 2011), we performed control experiments by injecting saline and corrected the D-glucose, 3OMG and L-glucose curves by division with the saline curve. Corrected and uncorrected curves are shown in Supplementary Figs. 6 and 7.

## 2.8. Protocols of substrate administration

In this study, four protocols of substrate administration were used. The glucose protocol (GP): 120  $\mu\text{l}$  50% w/v D-glucose (2.78 M) injected IV in one minute; the trans-acceleration protocol (TP): 120  $\mu\text{l}$  3 M 3OMG

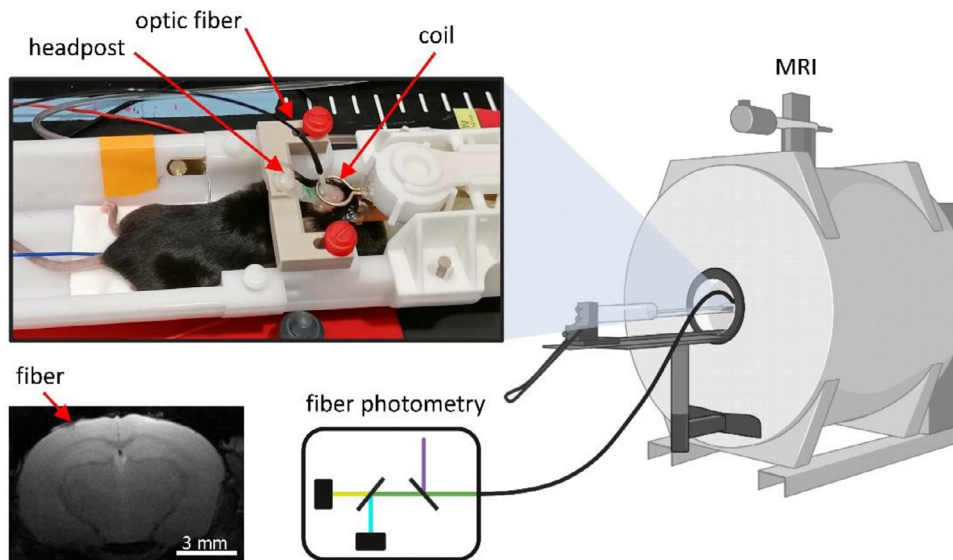


**Fig. 1.** Simultaneous MRI and fiber photometry setup. Mouse fixed in the custom-made MRI bed with chronically implanted headpost and optic fiber; T2 weighted anatomical image of the brain. The arrow indicates the susceptibility artifact caused by the fiber implant that was used to choose the imaged section.

injected IV in one minute; the L-glucose protocol (LP): 120  $\mu\text{l}$  50% w/v L-glucose (2.78 M) injected IV in one minute and the saline control protocol (SP): 120  $\mu\text{l}$  0.9% NaCl injected IV in one minute.

### 2.9. Kinetic modeling

The following equations were used to model glucose transport and metabolism, according to Duarte et al. (2009):

$$\frac{d([Glc]_{tissue})}{dt} = \frac{1}{V_{tissue}} [v_{blood/tissue} - CMR_{glc}]$$

$$v_{blood/tissue} = \frac{v_{max}}{K_m + [Glc]_{blood} + [Glc]_{tissue} + \frac{[Glc]_{blood}[Glc]_{tissue}}{K_{ii}}} ([Glc]_{blood} - [Glc]_{tissue})$$

Where  $[Glc]_{blood}$  and  $[Glc]_{tissue}$  are the glucose concentrations in the blood and tissue compartments, in ( $\text{mol} \cdot \text{L}^{-1}$ ),  $v_{max}$  is the maximum transport rate (in  $\text{mol} \cdot \text{s}^{-1}$ ),  $K_m$  and  $K_{ii}$  are the Michaelis and iso-inhibition constants.

The total simulation volume was set to 1  $\text{cm}^3$ . The relative volume of the extravascular space was set to 1% or 5%. The values of  $CMR_{glc}$ ,  $K_m$  and  $K_{ii}$  were set, respectively to 6.5  $\text{mM/s}$ , 5  $\text{mM}$  and 21  $\text{mM}$  (Barros et al., 2007). The value of  $v_{max}$  was calculated such that at the steady state blood concentration of 5  $\text{mM}$  (before injection) the glucose concentration in the tissue is 1  $\text{mM}$  (Duarte et al., 2009).

## 3. Results

### 3.1. Validation of FRET fiber photometry of glucose by 2PLSM

To perform simultaneous DGE and fiber photometry experiments, we designed a custom-made mouse holder that could be inserted into an MRI scanner while allowing sufficient space to accommodate the optic fiber without excessive bending (Fig. 1). The site of implantation was visible in the anatomical MRI images, ensuring that the tomographic data could be collected from the same brain volume that was sampled by photometry (Fig. 1). However, before being used for comparison with DGE MRI, ratiometric fiber photometry of glucose (Fig. 2A and B) requires an independent validation, since potential artifacts arising from fiber or brain autofluorescence might affect both the absolute values and the dynamics of the response.

Thus, to confirm the reliability of our fiber photometry results we performed 2PLSM imaging of neuronal and astrocytic glucose levels

(Fig. 2C and 2D, respectively) upon 1 min IV injection of 120  $\mu\text{l}$  50% w/v D-glucose. The dynamics of neuronal and astrocytic glucose concentration changes relative to baseline ( $R/R_{BL}$ ), are seen in Fig. 2E and F. In 2PLSM (black curves) both cell types show an increase in the relative FRET ratio,  $R/R_{BL}$ , and a slow gradual reduction after around an hour. Neurons reach the maximum change of 23% in 50–60 min and astrocytes reach a maximum change of 30% in 40 min after injection.

The fiber photometry curves (Fig. 2E and F, red traces), show a temporal profile similar to the 2PLSM curves (Fig. 2E and F, black traces), but with a reduced response amplitude. On average, neurons and astrocytes reach a maximum of 19% and 15%, respectively. The minor discrepancy in the neuronal traces might be due to instrumental factors, such as differences in the detected wavelength ranges, scattering and reabsorption effects or nature of the excitation (one-photon vs two-photon). However, the discrepancy is more pronounced for the astrocytic traces, suggesting additional biasing factors.

A potential explanation for this observation is a larger relative contribution of brain autofluorescence to the astrocytic signal. In fact, we used a lower viral titer for astrocytic expression compared to neuronal, due to the observation of neuronal protein expression using the GFAP promoter at higher AAV titers (Supplementary Fig. 3), in accordance with previous reports (Taschenberger et al., 2017). Since in fiber photometry cell specificity is only due to selective expression, the presence of a significant neuronal fraction would have compromised the results.

To overcome this problem, we tried a previously reported microRNA-based neuronal detargeting approach (Humbel et al., 2021; Taschenberger et al., 2017), producing two alternative sequences (Supplementary Fig. 4) in which the microRNA targeting part was inserted in different positions. An enhanced GFAP promoter, G1B3, was used to counteract a decrease in astrocytic expression (Humbel et al., 2021). Unfortunately, both sequences resulted in a much-reduced astrocytic expression and were thus not usable in our study (Supplementary Fig. 5).

Despite the remaining discrepancies, our comparison shows that fiber photometry of the glucose sensor FLIIP produces curves that have a very similar kinetic profile with respect to 2PLSM and thus provide a reliable semi-quantitative readout of the cellular uptake when combined with DGE MRI.

### 3.2. DGE and fiber photometry upon administration of D-glucose

To evaluate the feasibility of simultaneous DGE MRI and FRET fiber photometry of glucose, we first injected D-glucose intravenously, using the same protocol as in the validation experiments. The DGE MRI signal

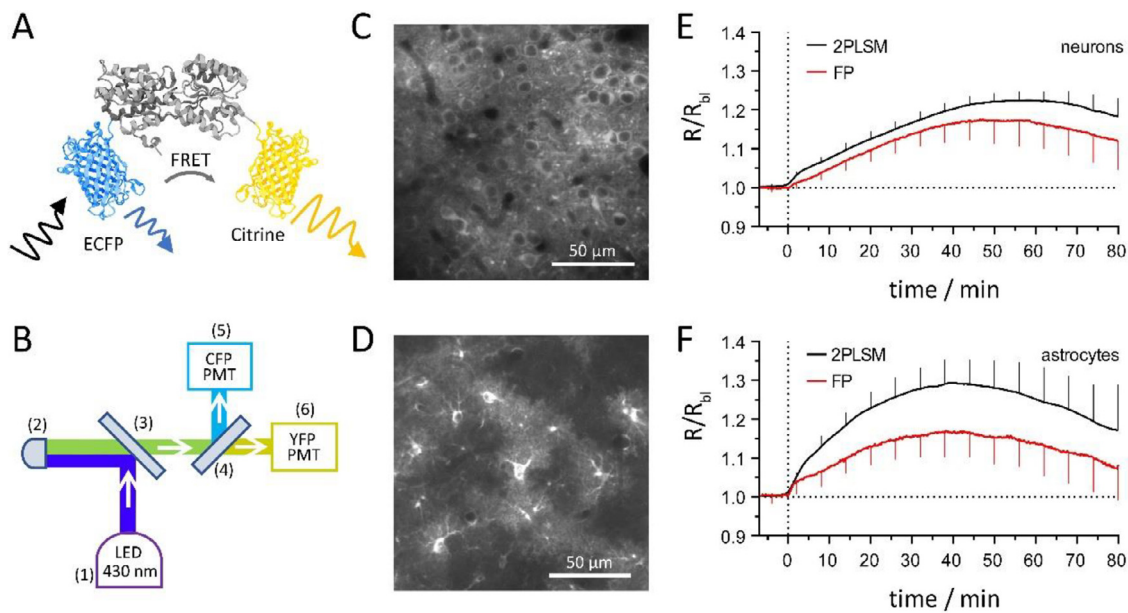


**Fig. 2.** (A) Molecular structure of the FRET glucose sensor FLIIP featuring ECFP as donor and Citrine as acceptor; (B) FRET fiber photometry setup: (1) Light source LED 430 nm, (2) Collimator, (3,4) dichroic mirrors, (5,6) photomultiplier tubes; (C,D) 2PLSM image of neuronal (C) and astrocytic (D) expression; (E,F) Comparison of 2PLSM and fiber photometry (FP) upon injection of D-glucose (at timepoint 0 min) for neurons (2PLSM  $n = 9$ ,  $N = 3$ ; FP  $n = 9$ ,  $N = 3$ ) (E) and astrocytes (2PLSM  $n = 10$ ,  $N = 4$ ; FP  $n = 9$ ,  $N = 3$ ) (F). Data are reported as mean  $\pm$  SD.

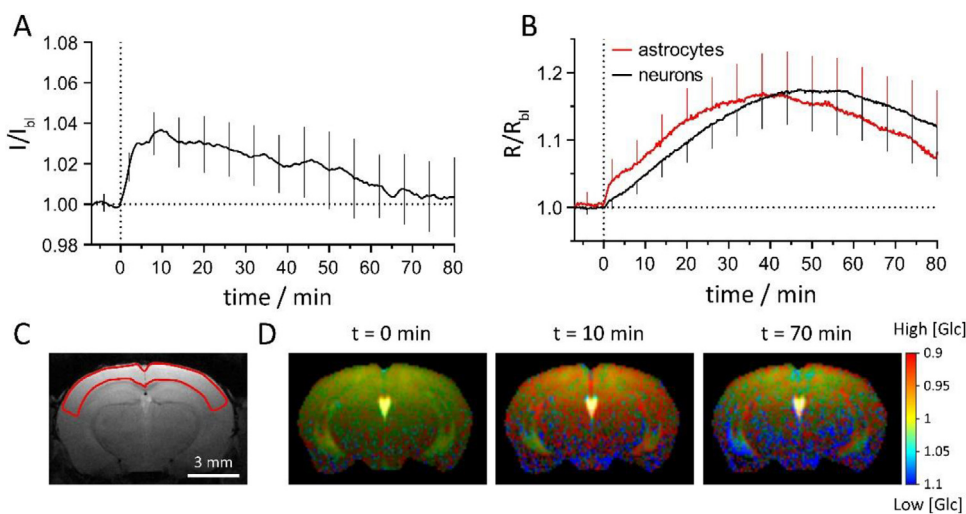


**Fig. 3.** DGE MRI from ROI in (C) ( $n = 18$ ,  $N = 6$ ) (A) and fiber photometry (B) in neurons ( $n = 9$ ,  $N = 3$ ) and astrocytes ( $n = 9$ ,  $N = 3$ ) upon injection of D-glucose (at timepoint 0 min). Anatomical image and ROI (C) and DGE contrast images at three time points (baseline, 10 min and 70 min post injection) (D). Data are reported as mean  $\pm$  SD.

and the simultaneously acquired fiber photometry measurements of the relative FRET ratio are shown in Fig. 3. The DGE MRI signal has a fast increase reaching a maximum of 3% 4 min after the start of the injection, followed by a steady decrease over the remaining 80 min (Fig. 3A). The astrocytic fluorescence ratio reaches a maximum of 17% at around 40 min post injection and the neuronal one reaches a maximum of 18% in around 50 min, consistently with two-photon data (Fig. 3B). The slower kinetics of glucose changes in both cell types suggest that the DGE signal cannot have only intracellular origin, especially in the first few minutes after injection.

To understand whether the brain extracellular space might be the main contributor to the DGE signal at short times after injection, we modelled the distribution of glucose between the blood and the brain tissue, considered as a single compartment containing both the extracellular space and the cells. To model the transport across the blood brain barrier, we used the simple carrier model, in which the GLUT transporter can alternate between four different states (Fig. 4A). This

model has proven successful in describing glucose transport in the brain in MRI studies (Duarte et al., 2009), and thus is particularly appropriate to interpret DGE signals. To generate input data for the modeling, we fitted experimental blood glucose data upon i.v. injection with a single exponential decay convoluted with a Gaussian function (Fig. 4B). Kinetic parameters for the transporters were chosen based on the previous study by Duarte et al. (2009). The calculated tissue concentrations are shown in Supplementary Fig. 8 for relative vascular volumes of 1 and 5%. The curves are minimally different, showing that our conclusions do not depend on the choice of the relative blood volume. To quantitatively interpret the DGE signal, the concentrations in each compartment should be weighted by their relative volumes and by differences in DGE signal due to e.g. pH or blood flow. While this is not feasible, it is still possible to use the normalized curves to analyze if the shape of the DGE curve is compatible with a signal originating only from the extravascular space (Fig. 4C). The experimental curve is well reproduced by a combination of vascular and extravascular signals, but clearly not by the

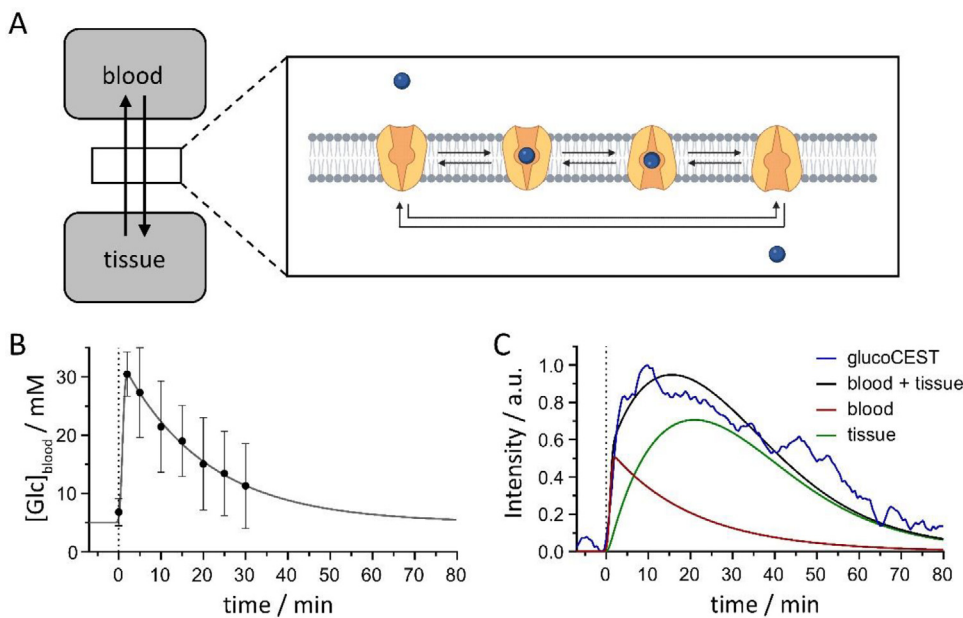


**Fig. 4.** (A) Schematic representation of the two-compartment kinetic model of glucose transport and metabolism in the brain, based on a four-state simple carrier model of the GLUT1 transporter. (B) Experimental blood glucose concentration (dots with SD interval) upon i.v. injection of D-glucose (50% w/v, 75  $\mu$ L, 1 min,  $n = 3$ ,  $N = 3$ ), fitted with an arbitrary function (solid line) to produce a smooth curve for modeling. (C) Fitting of the normalized DGE signal with the kinetic traces for blood and brain tissue glucose concentration obtained from modeling (with root mean square error RMSE = 0.0980, compared to RMSE = 0.2932 when fitting DGE only with the kinetic trace of blood (Supplementary Fig. 9)), showing that a vascular component is needed to account for the initial steep increase in DGE.

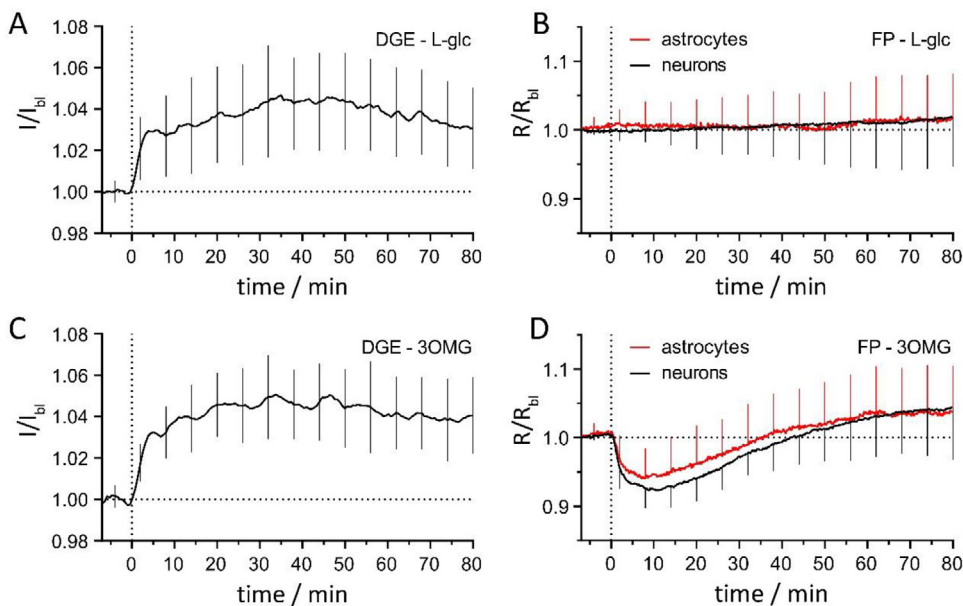


**Fig. 5.** DGE MRI ( $n = 21$ ,  $N = 13$ ) (A,C) and fiber photometry (FP) (B,D) in neurons and astrocytes upon injection of L-glucose (A,B) and 3OMG (C,D) (at timepoint 0 min). L-glucose: DGE ( $n = 19$ ,  $N = 13$ ), FP neurons ( $n = 10$ ,  $N = 7$ ), FP astrocytes ( $n = 9$ ,  $N = 6$ ). 3OMG: DGE ( $n = 21$ ,  $N = 13$ ), FP neurons ( $n = 9$ ,  $N = 6$ ), FP astrocytes ( $n = 12$ ,  $N = 7$ ). Data are reported as mean  $\pm$  SD.

extravascular component alone, demonstrating that at short times after injection the signal is dominated by the vascular component.

### 3.3. DGE and fiber photometry upon administration of L-glucose and 3-O-methyl-D-glucose

To confirm the contribution of the vascular space, we injected L-glucose, that is not a substrate for GLUT1 and therefore unable to cross the blood brain barrier (i.v., 2.78 M, 120  $\mu$ L in 1 min). The results are shown in Fig. 5. In DGE MRI, there is an initial fast increase, similar to the one observed for D-glucose, and a subsequent plateau that remains stable until the end of the experiment (Fig. 5A), confirming the ability of DGE to detect vascular contributions. As expected, there is no significant signal change in fiber photometry, since L-glucose does not get transported by either GLUT1 (predominant in endothelial cells and astrocytes) or GLUT3 (predominant in neurons) (Fig. 5B).

To further show the complementarity between fiber photometry and MRI techniques, we injected 3OMG, a known glucoCEST contrast agent

(i.v. 3 M, 120  $\mu$ L in 1 min). The DGE curve and the relative glucose concentration changes in astrocytes and neurons upon injection are shown in Fig. 5. The DGE curve shows a fast increase upon injection, similar to the one after D-glucose injection, reaching a maximum about 4 min after injection (Fig. 5C). After that, the signal is almost stable for the remaining 80 min. In the fiber photometry measurements, a reduction in both astrocytic and neuronal glucose is observed, followed by a recovery phase, due to trans-acceleration (Fig. 5D). Since 3OMG is not sensed by FLIIP, only the glucose decrease is reported. The astrocytic signal decreases by 6% in 8 min and goes above baseline again after 35 min post injection. The neuronal signal decreases by 8% in 10 min after injection and crosses the baseline 40 min post injection. Importantly, the observation of trans-acceleration further confirms that the lack of response to L-glucose injection cannot be explained simply by the fact that FLIIP is not sensitive to L-glucose. In fact, if L-glucose would pass through GLUTs, a reduction in the signal would be observed due to trans-acceleration, similarly to the 3OMG case.

#### 4. Discussion

In this study, we demonstrated the simultaneous acquisition of dynamic glucose-enhanced (DGE) MRI and FRET fiber photometry measurements of intracellular glucose concentration. The reliability of FRET fiber photometry for reporting changes of cell-specific glucose concentration was validated by comparison with 2PLSM. While the ratiometric response of the glucose sensor FLIIP in fiber photometry had a lower amplitude than in 2PLSM, the kinetic profile was similar, proving that the technique can effectively help elucidate the compartmental origin of the signal in DGE MRI experiments. In particular, the astrocytic expression of the sensor shows a lack of specificity that forced us to lower the expression levels, which in turn decreased signal intensity and rendered the measurement more susceptible to artifacts. The problem of increasing the reliability of astrocytic measurements in FRET fiber photometry might thus require more advanced approaches. Possible solutions could be the development of brighter sensors based on improved ECFP variants (Erard et al., 2013; Goedhart et al., 2012; Markwardt et al., 2011) or the use of mouse lines expressing either recombinase enzymes or directly the genetically encoded sensor (GES) of interest in astrocytes (Branda and Dymecki, 2004; Navabpour et al., 2020).

The simultaneous recording of FRET fiber photometry and DGE MRI traces allows to investigate the compartmental origin of the DGE signal. In particular, an initial sharp increase in the DGE signal was observed upon bolus injection of either D-glucose, 3OMG or L-glucose, but not in FRET fiber photometry. In the case of D-glucose, the only analyte that can be optically sensed, the fiber photometry curves show a much slower increase, followed by a decrease at longer timescale. This suggests that the initial sharp rise in DGE originates from the extracellular space of brain tissue and/or from the vasculature. While the former (together with the intracellular component) is commonly assumed as the origin of the DGE signal, the presence of a vascular component is currently debated. Some studies include this possibility, but argue that its contribution is lower than the one from the tissue compartment, because of its lower relative volume and because of blood flow, that induces a dilution of the glucose polarization (Chan et al., 2012; Huang et al., 2020). Nasrallah et al. (2013) reported the absence of a glucoCEST response upon injection of L-glucose, which cannot cross the blood brain barrier and thus remains intravascular. We failed to reproduce this observation in the present study. We observed an initial rise of the DGE signal upon L-glucose injection, similar to that obtained from D-glucose. The main difference between our study and that of Nasrallah et al. (2013) is the use of DGE over glucoCEST. The different analysis procedure in the two methods could be the source of the discrepancy between the results. In glucoCEST, using asymmetry analysis and normalization at an off-resonance chemical shift, the known symmetric T2 effect of OH groups of glucose at high dosage (Gore et al., 1986; Yadav et al., 2014) is largely eliminated. In DGE, the signal is normalized by the mean baseline, thus the T2 glucose effect is not canceled out. In our study, DGE was the method of choice, given that the aim was to both maximize signal changes and opt for high temporal resolution. Moreover, we used kinetic modeling to show that the initial fast rise upon D-glucose injection must include a significant vascular component.

Here we notice that even though the relative volume of the cerebral vasculature is only around 1% of the total brain volume in the murine cortex (Tsai et al., 2009), the concentration of D-glucose in the blood after an IV bolus injection of 75  $\mu$ L of 1.5 g/kg D-glucose increases by about 25 mM compared to baseline (Supplementary Fig. 8), which would correspond to a volume averaged increase of roughly 0.4–0.45 mM in our protocol, a concentration change that should be detectable by DGE. In addition, the consideration that the blood flow effect would reduce the glucoCEST signal was based on the fast flow rate in arteries (Knutsson et al., 2018), while the flow in the cortical capillary bed is known to be much slower (Schmid et al., 2017). Nevertheless, glucoCEST is susceptible to artifacts (Zaiss et al., 2019b) and we cannot completely rule out a spurious origin of the initial fast DGE response.

In any case, the comparison with FRET fiber photometry clearly speaks against a significant intracellular contribution at early time points after injection.

The strength of concurrent MRI and fiber photometry was further demonstrated in the experiments using 3OMG, a known DGE contrast agent (Rivlin and Navon, 2018; Sehgal et al., 2019). The DGE response showed a rapid rise followed by a plateau, similarly to what was observed for L-glucose. In contrast to L-glucose, 3OMG is a substrate for GLUTs and therefore an exchange between the vascular, extracellular and intracellular compartments is expected. This was demonstrated by the trans-acceleration effect observed by fiber photometry. Trans-acceleration is a well-characterized effect displayed by facilitated transporters like GLUTs and monocarboxylate transporters (Carruthers, 1990; Deng et al., 2014; Garcia et al., 1994; Miller, 1965; Widdas, 1952). The extracellular presence of transporter substrates, in this case 3OMG, stimulates a conformational switch of the transporter, moving the substrate binding site towards the intracellular compartment, thus facilitating the efflux of glucose. The difference between DGE MRI and FLIIP kinetics upon 3OMG injection indicates that the DGE signal is the sum of two temporal profiles, one due to 3OMG itself and one of opposite sign due to glucose. As a consequence, the interpretation of the DGE signal is not straightforward and caution is advised. Importantly, the 3OMG induced depletion of intracellular glucose concentration needs to be taken into consideration for potential clinical applications, especially in patients with metabolic disorders.

#### 5. Conclusions

In this work, we have introduced the combination of DGE MRI and FRET-based fiber photometry. By comparison with 2PLSM, we have shown that FRET fiber photometry of GESs presents several specific challenges but provides a qualitatively reliable temporal response. In particular, the possibility to target specific cell types generates compartment-specific data, which is not possible with glucoCEST or DGE because of the limited spatial resolution of MR techniques. The exact origin of the glucoCEST and DGE signal remains elusive, but our multimodal approach differentiated the relative contribution of different brain compartments. In conclusion, our study demonstrates the feasibility to combine quantitative photometric techniques with tomographic approaches and that this combination provides complementary information that can guide the interpretation of dynamic MR signals.

#### Data and code availability

The code utilized for the analysis of the DGE experiments is available at the following page: <https://gitlab.com/einlabzurich/dgeanalysis>. The code for the analysis of FRET and fiber photometry traces will be made available on the Experimental Imaging and Neuroenergetics GitLab page: <https://gitlab.com/einlabzurich/>. All data included in this study are available on Zenodo (doi:10.5281/zenodo.7382463).

A.E. and L.R. built and validated the fiber photometry setup; A.E. performed surgical procedures under the supervision of M.T.W. and G.W.; A.E. performed all experiments under the supervision of L.R. and A.S.; A.E., M.Z. and L.R. wrote the code for DGE, microscopy and photometry data analysis; A.E. performed data analysis under the supervision of L.R. and M.Z.; M.T.W. and B.W. conceived the project; all authors participated in writing the manuscript.

#### Declaration of Competing Interest

All authors report no potential conflicts of interest.

#### Data availability

Data will be made available on request.

## Acknowledgment

The authors would like to thank Sergei Vinogradov for kindly providing the acquisition software for the fiber photometry setup, Helmut Merkle for providing the surface coil and Felipe Barros for helpful discussions. Figs. 1, 3A and 4A were created with BioRender.com. This work was supported by funding from the European Union's Horizon 2020 research and innovation program under the Grant Agreement No 667510.

## References

- Anemone, A., Capozza, M., Arena, F., Zullino, S., Bardini, P., Terreno, E., Longo, D.L., Aime, S., 2021. *In vitro* and *in vivo* comparison of MRI chemical exchange saturation transfer (CEST) properties between native glucose and 3-O-Methyl-D-glucose in a murine tumor model. *NMR Biomed.* 34. doi:10.1002/nbm.4602.
- Barros, L.F., Bittner, C.X., Loaiza, A., Porras, O.H., 2007. A quantitative overview of glucose dynamics in the gliovascular unit. *Glia* 55, 1222–1237. doi:10.1002/glia.
- Brandt, C.S., Dymek, S.M., 2004. Talking about a revolution: the impact of site-specific recombinases on genetic analyses in mice. *Dev. Cell* 6, 7–28. doi:10.1016/S1534-5807(03)00399-X.
- Carruthers, A., 1990. Facilitated diffusion of glucose. *Physiol. Rev.* 70. doi:10.1152/physrev.1990.70.4.1135.
- Chan, K.W.Y., McMahon, M.T., Kato, Y., Liu, G., Bulte, J.W.M., Bhujwala, Z.M., Artemov, D., van Zijl, P.C.M., 2012. Natural D-glucose as a biodegradable MRI contrast agent for detecting cancer. *Magn. Reson. Med.* 68, 1764–1773. doi:10.1002/mrm.24520.
- Deng, D., Xu, C., Sun, P., Wu, J., Yan, C., Hu, M., Yan, N., 2014. Crystal structure of the human glucose. *Nature* 121–125. doi:10.1038/nature13306.
- Duarte, J.M.N., Morgenthaler, F.D., Lei, H., Poitry-Yamate, C., Gruetter, R., 2009. Steady-state brain glucose transport kinetics re-evaluated with a four-state conformational model. *Front. Neuroener.* 1, 1–10. doi:10.3389/neuro.14.006.2009.
- Erard, M., Fredj, A., Pasquier, H., Beltolngar, D.B., Bousmah, Y., Derrien, V., Vincent, P., Merola, F., 2013. Minimum set of mutations needed to optimize cyan fluorescent proteins for live cell imaging. *Mol. Biosyst.* 9, 258–267. doi:10.1039/c2mb25303h.
- Foerster, B.U., Tomasi, D., Caparelli, E.C., 2005. Magnetic field shift due to mechanical vibration in functional magnetic resonance imaging. *Magn. Reson. Med.* 54, 1261–1267. doi:10.1002/mrm.20695.
- Garcia, C.K., Goldstein, J.L., Pathak, R.K., Anderson, R.G.W., Brown, M.S., 1994. Molecular characterization of a membrane transporter for lactate, pyruvate, and other monocarboxylates: implications for the Cori cycle. *Cell* 76, 865–873. doi:10.1016/0092-8674(94)90361-1.
- Goedhart, J., Von Stetten, D., Noirclerc-Savoye, M., Lelimosin, M., Joosen, L., Hink, M.A., Van Weeren, L., Gadella, T.W.J., Royant, A., 2012. Structure-guided evolution of cyan fluorescent proteins towards a quantum yield of 93%. *Nat. Commun.* 3. doi:10.1038/ncomms1738.
- Gore, J.C., Brown, M.S., Mizumoto, C.T., Armitage, I.M., 1986. Influence of Glycogen on Water Proton Relaxation Times. *Magnetic Resonance in Medicine* doi:10.1002/mrm.1910030312.
- Gunaydin, L.A., Grosnick, L., Finkelstein, J.C., Kauvar, I.V., Fenno, L.E., Adhikari, A., Lammel, S., Mirzabekov, J.J., Airan, R.D., Zalocusky, K.A., Tye, K.M., Anikeeva, P., Malenka, R.C., Deisseroth, K., 2014. Natural neural projection dynamics underlying social behavior. *Cell* 157, 1535–1551. doi:10.1016/j.cell.2014.05.017.
- Herholz, K., Coope, D., Jackson, A., 2007. Metabolic and molecular imaging in neuro-oncology. *Lancet Neurol.* 6, 711–724. doi:10.1016/S1474-4422(07)70192-8.
- Holtmaat, A., Bonhoeffer, T., Chow, D.K., Chuckowree, J., Paola, V.De, Keck, T., Knott, G., Lee, W.A., Mostany, R., Hofer, S.B., Huebener, M., Mrcsic-flogel, T.D., Nedivi, E., Portera-Cailliau, C., Svoboda, K., Trachtenberg, J.T., Wilbrecht, L., 2009. Long-term, high-resolution imaging in the mouse neocortex through a chronic cranial window. *Nat. Protoc.* 4, 1128–1144. doi:10.1038/nprot.2009.89.
- Huang, J., van Zijl, P.C.M., Han, X., Dong, C.M., Cheng, G.W.Y., Tse, K.H., Knutsson, L., Chen, L., Lai, J.H.C., Wu, E.X., Xu, J., Chan, K.W.Y., 2020. Altered d-glucose in brain parenchyma and cerebrospinal fluid of early Alzheimer's disease detected by dynamic glucose-enhanced MRI. *Sci. Adv.* 6, 1–10. doi:10.1126/sciadv.aba3884.
- Humbel, M., Ramosaj, M., Zimmer, V., Regio, S., Aeby, L., Moser, S., Boizot, A., Sipion, M., Rey, M., Déglon, N., 2021. Maximizing lentiviral vector gene transfer in the CNS. *Gene Ther.* 28, 75–88. doi:10.1038/s41434-020-0172-6.
- Jin, T., Mehrens, H., Wang, P., Kim, S.G., 2018. Chemical exchange-sensitive spin-lock MRI of glucose analog 3-O-methyl-d-glucose in normal and ischemic brain. *J. Cereb. Blood Flow Metab.* 38, 869–880. doi:10.1177/0271678X17707419.
- Jones-Tabah, J., Mohammad, H., Clarke, P.B., Hebert, T.E., 2021. *In vivo* detection of GPCR-dependent signaling using fiber photometry and FRET-based biosensors. *Methods* 1–18. doi:10.1016/j.ymeth.2021.05.002.
- Jones-Tabah, J., Mohammad, H., Hadj-Youssef, S., Kim, L.E.H., Martin, R.D., Benaliouaf, F., Tanny, J.C., Clarke, P.B.S., Hébert, T.E., 2020. Dopamine D1 receptor signalling in dyskinetic Parkinsonian rats revealed by fiber photometry using FRET-based biosensors. *Sci. Rep.* 10, 1–18. doi:10.1038/s41598-020-71121-8.
- Kim, M., Eleftheriou, A., Ravotto, L., Weber, B., Rivlin, M., Navon, G., Capozza, M., Anemone, A., Livio, D., Silvio, L., Moritz, A., Herz, K., Deshmane, A., Lindig, T., Bender, B., Golay, X., 2022. What do we know about dynamic glucose enhanced (DGE) MRI and how close is it to the clinics? Horizon 2020 GLINT consortium report. *Magnetic Resonance Materials in Physics. Biol. Med.* 35, 87–104. doi:10.1007/s10334-021-00994-1.
- Knutsson, L., Seidemo, A., Rydhög Scherman, A., Markenroth Bloch, K., Kalyani, R.R., Andersen, M., Sundgren, P.C., Wirestam, R., Helms, G., van Zijl, P.C.M., Xu, X., 2018. Arterial input functions and tissue response curves in dynamic glucose-enhanced (DGE) imaging: comparison between glucoCEST and blood glucose sampling in humans. *Tomography* 4, 164–171. doi:10.18383/j.tom.2018.00025.
- Komatsubara, A.T., Matsuda, M., Aoki, K., 2015. Quantitative analysis of recombination between YFP and CFP genes of FRET biosensors introduced by lentiviral or retroviral gene transfer. *Sci. Rep.* 5, 1–10. doi:10.1038/srep13283.
- Lange, T., Zaitsev, M., Buechert, M., 2011. Correction of frequency drifts induced by gradient heating in 1H spectra using interleaved reference spectroscopy. *J. Magn. Reson. Imaging* 33, 748–754. doi:10.1002/jmri.22471.
- Langen, K.J., Galldiks, N., Hattingen, E., Shah, N.J., 2017. Advances in neuro-oncology imaging. *Nat. Rev. Neurol.* 13, 279–289. doi:10.1038/nrneuro.2017.44.
- Liang, Z., Ma, Y., Watson, G.D.R., Zhang, N., 2017. Simultaneous GCaMP6-based fiber photometry and fMRI in rats. *J. Neurosci. Methods* 289, 31–38. doi:10.1016/j.jneumeth.2017.07.002.
- Markwardt, M.L., Kremers, G.J., Kraft, C.A., Ray, K., Cranfill, P.J.C., Wilson, K.A., Day, R.N., Wachter, R.M., Davidson, M.W., Rizzo, M.A., 2011. An improved cerulean fluorescent protein with enhanced brightness and reduced reversible photoswitching. *PLoS One* 6. doi:10.1371/journal.pone.0017896.
- Mayrhofer, J.M., Haiss, F., Haenni, D., Weber, S., Zwend, M., Barrett, M.J.P., Ferrari, K.D., Maechler, P., Saab, A.S., Stobart, J.L., Wyss, M.T., Johannssen, H., Osswald, H., Palmer, L.M., Revol, V., Schuh, C.-D., Urban, C., Hall, A., Larkum, M.E., Rutz-Innerhofer, E., Zeilhofer, H.U., Ziegler, U., Weber, B., 2015. Design and performance of an ultra-flexible two-photon microscope for *in vivo* research. *Biomed. Opt. Express.* 6, 4228. doi:10.1364/boe.6.004228.
- Miller, D.M., 1965. The kinetics of selective biological transport. II. Equations for induced uphill transport of sugars in human erythrocytes. *Biophys. J.* 5, 417–423. doi:10.1016/S0006-3495(65)86726-1.
- Nasrallah, F.A., Pagès, G., Kuchel, P.W., Golay, X., Chuang, K.H., 2013. Imaging brain deoxyglucose uptake and metabolism by glucoCEST MRI. *Journal of Cerebral Blood Flow & Metabolism* 33 (8), 1270–1278. doi:10.1038/jcbfm.2013.79.
- Natsubori, A., Tsunematsu, T., Karashima, A., Imamura, H., Kabe, N., Trevisiol, A., Hirrlinger, J., Kodama, T., Sanagi, T., Masamoto, K., Takata, N., Nave, K.A., Matsui, K., Tanaka, K.F., Honda, M., 2020. Intracellular ATP levels in mouse cortical excitatory neurons varies with sleep-wake states. *Commun. Biol.* 3, 1–5. doi:10.1038/s42003-020-01215-6.
- Navabpour, S., Kwapis, J.L., Jarome, T.J., 2020. A neuroscientist's guide to transgenic mice and other genetic tools. *Neurosci. Biobehav. Rev.* 108, 732–748. doi:10.1016/j.neubiorev.2019.12.013.
- Patel, A.A., McAlinden, N., Mathieson, K., Sakata, S., 2020. Simultaneous electrophysiology and fiber photometry in freely behaving mice. *Front. Neurosci.* 14, 1–9. doi:10.3389/fnins.2020.00148.
- Paterna, J.-C., Feldon, J., Büeler, H., 2004. Transduction profiles of recombinant adeno-associated virus vectors derived from serotypes 2 and 5 in the nigrostriatal system of rats. *J. Virol.* 78, 6808–6817. doi:10.1128/jvi.78.13.6808-6817.2004.
- Pisanello, M., Pisanò, F., Hyun, M., Maglie, E., Balena, A., De Vittorio, M., Sabatini, B.L., Pisanello, F., 2019. The three-dimensional signal collection field for fiber photometry in brain tissue. *Front. Neurosci.* 13, 1–16. doi:10.3389/fnins.2019.00082.
- Pologruto, T.A., Sabatini, B.L., Svoboda, K., 2003. ScanImage: flexible software for operating laser scanning microscopes. *Biomed. Eng. Online* 2, 13. doi:10.1186/1475-925X-2-13.
- Pradier, B., Wachsmuth, L., Nagelmann, N., Segelcke, D., Kreitz, S., Hess, A., Pogatzki-Zahn, E.M., Faber, C., 2021. Combined resting state-fMRI and calcium recordings show stable brain states for task-induced fMRI in mice under combined ISO/MED anesthesia. *Neuroimage* 245, 118626. doi:10.1016/j.neuroimage.2021.118626.
- Rivlin, M., Navon, G., 2018. CEST MRI of 3-O-methyl-D-glucose on different breast cancer models. *Magn. Reson. Med.* 79, 1061–1069. doi:10.1002/mrm.26752.
- Roussel, T., Frydman, L., Le Bihan, D., Ciobanu, L., 2019. Brain sugar consumption during neuronal activation detected by CEST functional MRI at ultra-high magnetic fields. *Sci. Rep.* 9, 1–11. doi:10.1038/s41598-019-40986-9.
- Sasaki, A., Nagatomo, K., Ono, K., Yamamoto, T., Otsuka, Y., Teshima, T., Yamada, K., 2016. Uptake of a fluorescent l-glucose derivative 2-NBDLG into three-dimensionally accumulating insulinoma cells in a phloretin-sensitive manner. *Hum. Cell* 29, 37–45. doi:10.1007/s13577-015-0125-3.
- Schmid, F., Tsai, P.S., Kleinfeld, D., Jenny, P., Weber, B., 2017. Depth-dependent flow and pressure characteristics in cortical microvascular networks. *PLoS Comput. Biol.* 13, 1–22. doi:10.1371/journal.pcbi.1005392.
- Schulz, K., Sydekum, E., Krueppel, R., Engelbrecht, C.J., Schlegel, F., Schröder, A., Rudin, M., Helmchen, F., 2012. Simultaneous BOLD fMRI and fiber-optic calcium recording in rat neocortex. *Nat. Methods* 9, 597–602. doi:10.1038/nmeth.2013.
- Sehgal, A.A., Li, Y., Lal, B., Yadav, N.N., Xu, X., Xu, J., Laterra, J., van Zijl, P.C.M., 2019. CEST MRI of 3-O-methyl-D-glucose uptake and accumulation in brain tumors. *Magn. Reson. Med.* 1993–2000. doi:10.1002/mrm.27489.
- Takanaga, H., Chaudhuri, B., Frommer, W.B., 2008. GLUT1 and GLUT9 as major contributors to glucose influx in HepG2 cells identified by a high sensitivity intracellular FRET glucose sensor. *Biochim. Biophys. Acta Biomembr.* 1778, 1091–1099. doi:10.1016/j.bbame.2007.11.015.
- Taschenberger, G., Tereshchenko, J., Kügler, S., 2017. A MicroRNA124 target sequence restores astrocyte specificity of gfaABC1D-driven transgene expression in AAV-mediated gene transfer. *Mol. Ther. Nucleic Acids* 8, 13–25. doi:10.1016/j.omtn.2017.03.009.
- Tolomeo, D., Micotti, E., Serra, S.C., Chappell, M., Snellman, A., Forloni, G., 2018. Chemical exchange saturation transfer MRI shows low cerebral 2-deoxy-D-glucose uptake in a model of Alzheimer's disease. *Sci. Rep.* 8, 9576. doi:10.1038/s41598-018-27839-7.
- Tsai, P.S., Kaufhold, J.P., Blinder, P., Friedman, B., Drew, P.J., Karten, H.J., Lyden, P.D., Kleinfeld, D., 2009. Correlations of neuronal and microvascular densities in murine

- cortex revealed by direct counting and colocalization of nuclei and vessels. *J. Neurosci.* 29, 14553–14570. doi:[10.1523/JNEUROSCI.3287-09.2009](https://doi.org/10.1523/JNEUROSCI.3287-09.2009).
- Tu, T.-W., Ibrahim, W.G., Jikaria, N., Munasinghe, J.P., Witko, J.A., Hammoud, D.A., Frank, J.A., 2018. On the detection of cerebral metabolic depression in experimental traumatic brain injury using chemical exchange saturation transfer (CEST) - weighted MRI. *Sci. Rep.* 8, 669. doi:[10.1038/s41598-017-19094-z](https://doi.org/10.1038/s41598-017-19094-z).
- van Zijl, P.C.M., Yadav, N.N., 2011. Chemical exchange saturation transfer (CEST): what is in a name and what isn't? *Magn. Reson. Med.* 65, 927–948. doi:[10.1002/mrm.22761](https://doi.org/10.1002/mrm.22761).
- Walker-Samuel, S., Ramasawmy, R., Torrealdea, F., Rega, M., Rajkumar, V., Johnson, S.P., Richardson, S., Gonçalves, M., Parkes, H.G., Årstad, E., Thomas, D.L., Pedley, R.B., Lythgoe, M.F., Golay, X., 2013. *In vivo* imaging of glucose uptake and metabolism in tumors. *Nat. Med.* 19, 1067–1072. doi:[10.1038/nm.3252](https://doi.org/10.1038/nm.3252).
- Wang, Y., DeMarco, E.M., Witzel, L.S., Keighron, J.D., 2021. A selected review of recent advances in the study of neuronal circuits using fiber photometry. *Pharmacol. Biochem. Behav.* 201. doi:[10.1016/j.pbb.2021.173113](https://doi.org/10.1016/j.pbb.2021.173113).
- Wang, Y.L., 2007. Noise-induced systematic errors in ratio imaging: serious artefacts and correction with multi-resolution denoising. *J. Microsc.* 228, 123–131. doi:[10.1111/j.1365-2818.2007.01834.x](https://doi.org/10.1111/j.1365-2818.2007.01834.x).
- Weiskopf, N., Edwards, L.J., Helms, G., Mohammadi, S., Kirilina, E., 2021. Quantitative magnetic resonance imaging of brain anatomy and *in vivo* histology. *Nat. Rev. Phys.* 3, 570–588. doi:[10.1038/s42254-021-00326-1](https://doi.org/10.1038/s42254-021-00326-1).
- Widdas, W.F., 1952. Inability of diffusion to account for placental glucose transfer in the sheep and consideration of the kinetics of a possible carrier transfer. *J. Physiol.* 23–39. doi:[10.1113/jphysiol.1952.sp004770](https://doi.org/10.1113/jphysiol.1952.sp004770).
- Xu, X., Chan, K.W.Y., Knutsson, L., Artemov, D., Xu, J., Liu, G., Kato, Y., Lal, B., Lattera, J., McMahon, M.T., van Zijl, P.C.M., 2015. Dynamic glucose enhanced (DGE) MRI for combined imaging of blood – brain barrier break down and increased blood volume in brain cancer. *Magn. Reson. Med.* 74, 1556–1563. doi:[10.1002/mrm.25995](https://doi.org/10.1002/mrm.25995).
- Xu, X., Sehgal, A.A., Yadav, N.N., Lattera, J., Blair, L., Blakeley, J., Seidemo, A., Coughlin, J.M., Pomper, M.G., Knutsson, L., van Zijl, P.C.M., 2020. D -glucose weighted chemical exchange saturation transfer (glucoCEST) -based dynamic glucose enhanced (DGE) MRI at 3T : early experience in healthy volunteers and brain tumor patients. *Magn. Reson. Med.* 84, 247–262. doi:[10.1002/mrm.28124](https://doi.org/10.1002/mrm.28124).
- Yadav, N.N., Xu, J., Bar-Shir, A., Qin, Q., Chan, K.W.Y., Grgac, K., Li, W., McMahon, M.T., van Zijl, P.C.M., 2014. Natural D-glucose as a biodegradable MRI relaxation agent. *Magn. Reson. Med.* 72, 823–828. doi:[10.1002/mrm.25329](https://doi.org/10.1002/mrm.25329).
- Yellen, G., Mongeon, R., 2015. Quantitative two-photon imaging of fluorescent biosensors. *Curr. Opin. Chem. Biol.* 27, 24–30. doi:[10.1016/j.cbpa.2015.05.024](https://doi.org/10.1016/j.cbpa.2015.05.024).
- Yu, L., Thurston, E.L.M.S., Hashem, M., Dunn, J.F., Whelan, P.J., Murari, K., 2020. Fiber photometry for monitoring cerebral oxygen saturation in freely-moving rodents. *Biomed. Eng. Online* 11, 3491–3506.
- Zaiss, M., Anemone, A., Goerke, S., Longo, D.L., Herz, K., Pohmann, R., Aime, S., Rivlin, M., Navon, G., Golay, X., Scheffler, K., 2019a. Quantification of hydroxyl exchange of D-Glucose at physiological conditions for optimization of glucoCEST MRI at 3, 7 and 9.4 Tesla. *NMR Biomed.* 32, e4113. doi:[10.1002/nbm.4113](https://doi.org/10.1002/nbm.4113).
- Zaiss, M., Herz, K., Deshmene, A., Kim, M., Golay, X., Lindig, T., Bender, B., Ernemann, U., Scheffler, K., 2019b. Possible artifacts in dynamic CEST MRI due to motion and field alterations. *J. Magn. Reson.* 298, 16–22. doi:[10.1016/j.jmr.2018.11.002](https://doi.org/10.1016/j.jmr.2018.11.002).
- Zhao, F.-Q., Keating, A.F., 2007. Functional properties and genomics of glucose transporters. *Curr. Genom.* doi:[10.2174/138920207780368187](https://doi.org/10.2174/138920207780368187).